

Research Article

Porous Activated Carbons Derived from *Pleurotus eryngii* for Supercapacitor Applications

Yudan Yuan ¹, Ruowei Yi,^{2,3} Yi Sun,^{4,5} Jianqiao Zeng,^{4,5} Jiaqi Li,^{4,5} Jiahao Hu,^{4,5} Yinchao Zhao,^{4,5} Wei Sun,⁶ Chun Zhao,^{4,5} Li Yang ^{2,3} and Cezhou Zhao ^{1,4,5}

¹School of Electronic and Information Engineering, Xi'an Jiaotong University, Xi'an 710049, China

²Department of Chemistry, Xi'an Jiaotong-Liverpool University, Suzhou 215123, China

³Department of Chemistry, University of Liverpool, Liverpool, UK

⁴Department of Electrical and Electronic Engineering, Xi'an Jiaotong-Liverpool University, Suzhou 215123, China

⁵Department of Electrical Engineering and Electronics, University of Liverpool, UK

⁶GMCC Electronic Technology Wuxi Co. Ltd., Wuxi 214000, China

Correspondence should be addressed to Li Yang; li.yang@xjtlu.edu.cn and Cezhou Zhao; cezhou.zhao@xjtlu.edu.cn

Received 27 December 2017; Revised 21 March 2018; Accepted 24 April 2018; Published 5 August 2018

Academic Editor: Ananthakumar Ramadoss

Copyright © 2018 Yudan Yuan et al. This is an open access article distributed under the Creative Commons Attribution License, which permits unrestricted use, distribution, and reproduction in any medium, provided the original work is properly cited.

Varieties of natural biomass have been utilized to prepare porous carbon materials for supercapacitor applications. In this work, porous activated carbons derived from *Pleurotus eryngii* were prepared by carbonization and KOH activation. The activated carbons presented a large specific surface area of $3255 \text{ m}^2 \cdot \text{g}^{-1}$ with high porosity. The as-prepared electrode exhibited a maximal specific capacitance of $236 \text{ F} \cdot \text{g}^{-1}$ measured in a three-electrode cell system. Furthermore, the assembled symmetric supercapacitor showed a specific capacitance of $195 \text{ F} \cdot \text{g}^{-1}$ at $0.2 \text{ A} \cdot \text{g}^{-1}$ and a superior specific capacitance retention of about 93% after 15000 cycles. The desirable capacitive behavior suggests that *Pleurotus eryngii* is an attractive biomass source of carbon materials for the potential supercapacitor applications.

1. Introduction

A supercapacitor is considered a promising energy storage device due to its unique merits of high specific power, high cycle stability, and rapid charge-discharge performance [1]. Owing to these features, a supercapacitor has been widely involved in various application fields, such as electric vehicles, consumer electronics, and industrial energy management [2, 3].

A large amount of electrode materials for supercapacitors has been investigated so far, including carbon materials [4–6], metal oxides [7, 8], and conducting polymers [9, 10]. In recent years, two-dimensional (2D) nanomaterials [11] and hybrid materials [12] have attracted great interests. However, the synthesis of 2D nanosheets and hybrid materials is commonly involved with methods like arc-discharge synthesis, chemical vapor deposition, and microwave radiation, which are expensive, complicated, and sometimes

harmful to the environment [13–15]. Now, the trend is to use biomass as a convenient and economical method for supercapacitors. Porous carbon material derived from biomass is regarded as one of the most promising candidates due to its high surface areas, good electrical conductivity, low cost, and renewability [16, 17].

Recently, varieties of natural biomass have been utilized as starting materials to prepare porous carbon materials for supercapacitor [18–20]. It was reported that willow catkins activated by KOH present large three-dimensional interconnected micrometer-level pores composed of sheet-like primary particles [20]. Five types of tea leaves prepared by high-temperature carbonization and activation with KOH show typical amorphous and porous structures with a high specific surface [21]. Furthermore, N-doped porous carbon microsphere materials, synthesized from fermented rice, offer high porosity and high capacitance [22].

Mushrooms, rich in carbon and oxygen, are widely distributed around the world. They are abundant, economical, and environmentally friendly. In this regard, many kinds of mushrooms have been used in supercapacitor applications [23, 24]. *Pleurotus eryngii*, a kind of mushrooms, has been commercially produced by the industrial process for decades with a considerable yield. This endows the *Pleurotus eryngii* with low price which helps it stand out among other biomass resources. Here, we reported a new facile way to synthesize the electrode materials with *Pleurotus eryngii* as a precursor.

In this work, a facile fabrication of porous activated carbons derived from *Pleurotus eryngii*, followed by carbonization and KOH activation, has been demonstrated. The obtained materials present a high specific surface area of $3255 \text{ m}^2 \cdot \text{g}^{-1}$. In a three-electrode cell system, the prepared electrode offers a maximal specific capacitance of $236 \text{ F} \cdot \text{g}^{-1}$. Furthermore, the assembled symmetric supercapacitor shows a specific capacitance of $195 \text{ F} \cdot \text{g}^{-1}$ at $0.2 \text{ A} \cdot \text{g}^{-1}$ and a superior specific capacitance retention of about 93% after 15000 cycles. This work highlights the attractive features of *Pleurotus eryngii* in a supercapacitor which might inspire their future development in new energy storage device prototypes.

2. Experiments

2.1. Material Synthesis. *Pleurotus eryngii* was firstly washed with ethanol and dried at 60°C overnight. Secondly, the dried *Pleurotus eryngii* was carbonized under a nitrogen atmosphere at 500°C for 12 hours. And then, the carbonized *Pleurotus eryngii* was mixed with KOH solution in a 1:3 weight ratio and dried at 120°C overnight in a vacuum oven. The mixture was subsequently activated under a nitrogen atmosphere at 600, 700, and 800°C , respectively. Finally, the activated sample was washed with hydrochloric acid solution and excessive distilled water to remove the impurities. The products were denoted as APE-*X*, where *X* was the activation temperature.

2.2. Material Characterization. The samples were examined under a scanning electron microscope (SEM, Hitachi S4700). The morphology images were recorded on a transmission electron microscope (TEM, FEI Tecnai G2 F20 S-twin TEM system). X-ray diffraction (XRD) patterns were measured on a Bruker D8 ADVANCE diffractometer. Raman spectra were examined by a Renishaw inVia Raman microscope. X-ray photoelectron spectroscopy (XPS) analysis was carried out on a Thermo Scientific XPS system. Specific surface areas of the samples were measured by the Brunauer-Emmett-Teller (BET) method on a Beishide 3H-2000PS2 specific surface and pore size analysis instrument.

2.3. Electrochemical Measurements. The electrochemical performance of the active materials was measured in both three-electrode and two-electrode systems with 6 M KOH aqueous solution used as the electrolyte. In the three-electrode system, the counter electrode and reference electrode were platinum foil and saturated Ag/AgCl. The working electrode was prepared by mixing the active materials (80 wt%), polyvinylidene fluoride (10 wt%), and carbon black (10 wt%) in a few

drops of N-methyl-2-pyrrolidone solvent. Subsequently, the resulting mixture was coated on a nickel foam substrate and dried at 80°C vacuum for 24 hours [25]. The mass loading of the active material for each electrode was about $5 \text{ mg} \cdot \text{cm}^{-2}$. In the two-electrode system, the symmetric supercapacitor was assembled by employing two APE-700 electrodes with a separator. The cyclic voltammetry (CV), galvanostatic charge/discharge (GCD), and electrochemical impedance spectroscopy (EIS) measurements were carried out on a Metrohm Autolab PGSTAT302N electrochemical workstation. The specific capacitance C_m ($\text{F} \cdot \text{g}^{-1}$) was calculated according to the discharge curve by the following equation [18, 26]:

$$C_m = \frac{k I \Delta t}{(m \Delta V)} \quad (1)$$

where I (A) is the discharge current, Δt (s) is the discharge time, ΔV (V) is the discharge voltage window excluding the IR drop, m (g) is the mass of active materials in a single electrode, and k is a constant ($k = 1$ for a three-electrode system and $k = 2$ for a two-electrode system).

3. Results and Discussions

As shown in the SEM image of Figure 1(a), the *Pleurotus eryngii* presents three-dimensional porous network structure with micrometer-level pores. Figures 1(b) and 1(c) show the carbonized samples with different magnifications. The SEM image of the activated samples at 700°C is displayed in Figure 1(d). When comparing Figures 1(c) and 1(d), it is found that a higher roughness is observed on the surface of the activated samples after KOH activation. The TEM image of APE-700 as shown in Figure 2(a) indicates that numerous nanoparticles are stacked each other in different directions aggregating on the rough surface of the activated samples (Figure 1(d)). A high-resolution TEM (Figure 2(b)) image from APE-700 reveals that less than 1 nm abundant micropores are created after the activation.

The XRD patterns of various temperature-activated samples are shown in Figure 3(a). All the APE samples exhibit two broad- and low-intensity peaks near 25° and 43° , corresponding to (002) and (100) planes of the graphite [25, 27]. The intensity of these two peaks decreases as the activation temperature increases, probably due to a lower graphitization degree [20]. Figures 3(b)–3(d) are the Raman spectra of APEs. Two broad bands centered at 1350 cm^{-1} (D-band) and 1584 cm^{-1} (G-band) are clearly observed [20, 25]. The relative intensity ratios of D-band to G-band (I_D/I_G) of APE-600, APE-700, and APE-800 are 2.9, 3.3, and 3.6, respectively. As the D-band is induced by the defects in the graphite lattice and the G-band is generated by the sp^2 carbon atomic pair stretching, APE-800 exhibits the lowest graphitization degree [28]. This can be ascribed to the higher temperature facilitating the erosion reaction between carbonaceous material and KOH, which may decrease the graphitization degree of the APE materials. The results are consistent with those of the XRD analysis in Figure 3(a).

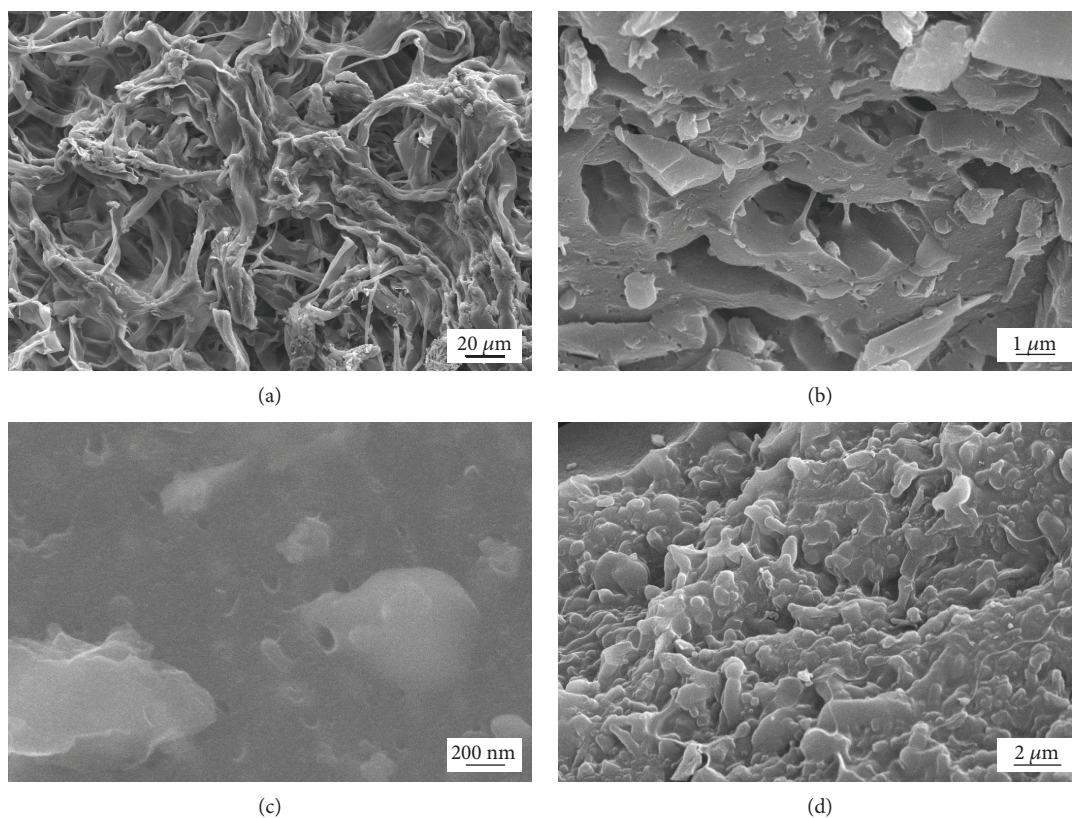


FIGURE 1: SEM images of (a) *Pleurotus eryngii*, (b, c) carbonized *Pleurotus eryngii* with different magnifications, and (d) as-prepared APE-700 electrode sample.

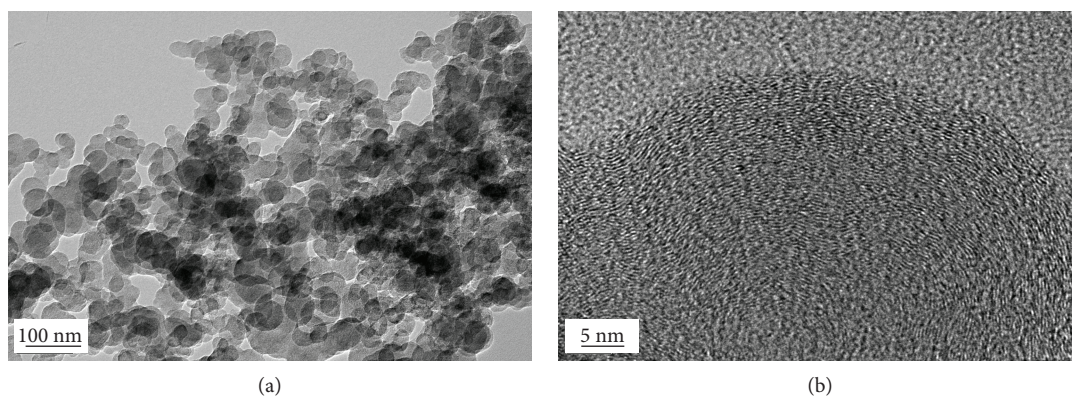


FIGURE 2: (a, b) TEM images of APE-700 with different magnifications.

XPS measurement was used to further confirm the surface chemical properties and atomic compositions of as-prepared APEs. The wide XPS spectra in Figure 4(a) display two peaks at 284 and 533 eV, corresponding to C 1s and O 1s, respectively. There are oxygen-containing functional groups in all the activated samples [25]. The atomic percentage of oxygen decreases from 17.33 to 8.91 atom% (see Table 1) when the activation temperature has been changed from 600°C to 800°C. The C 1s spectra of APEs in Figures 4(b)–4(d) could be approximately fitted into three peaks, which can be assigned to sp^2 C=C bond in graphitic carbon

(284.6 eV), sp^3 C-C hybridization (285.4 eV), and -C=O/-COO- bond (288.6 eV) [25, 29]. The relative intensity of sp^3 C-C hybridization peaks (the purple peaks in Figures 4(b)–4(d)) increases as the temperature raises from 600 to 800°C. The increasing intensity in the C-C bond corresponds to the reduction of the graphitization degree for APE samples at higher temperature. The most probable reason is that the KOH is more reactive with carbonaceous materials, which causes more lattice defects in the activation process.

The nitrogen adsorption-desorption isotherms of APEs activated at 600°C, 700°C, and 800°C are shown in

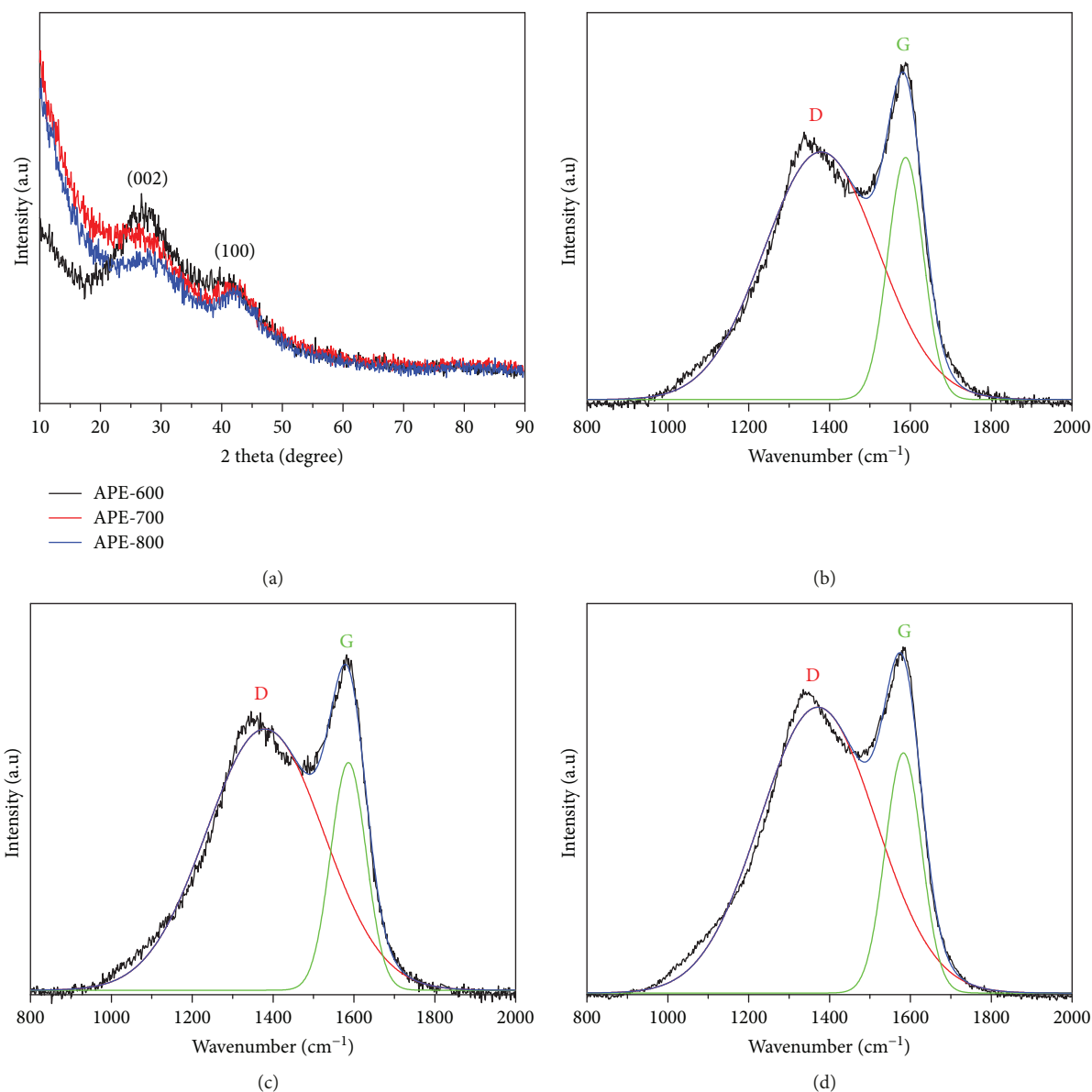
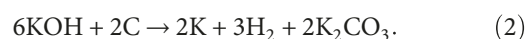


FIGURE 3: (a) XRD patterns of APEs obtained at various activation temperatures. Raman spectra of APE-600 (b), APE-700 (c), and APE-800 (d).

Figure 5(a). An abrupt increase occurs at very low relative pressure (less than 0.1) according to isotherms, followed by a smooth increase at the high relative pressures. From those results, it implies that the APEs have abundant micropores with a narrow pore size distribution [30]. At the relative pressures from 0.4 to 1.0, the subtle hysteresis loops provide evidence for forming a small amount of mesopores in the samples [31].

When the activation temperatures increase from 600°C to 700°C, the flat plateau of the isotherms, as shown in Figure 5(a), moves to a higher position, revealing that more pores are produced and, as a result, a higher specific surface area is achieved [32]. However, it can be noted that the plateau is shifted down when increasing the activation temperature to 800°C. A collapse of the pore structure may probably happen due to the excessive temperature. The total

BET specific surface area of APE-700 is 3255 m²·g⁻¹ with respect to 2253 m²·g⁻¹ for APE-600 and 2704 m²·g⁻¹ for APE-800. The mechanism of KOH activation is shown in the following equation [23, 33]:



During the KOH activation process, the carbon frameworks are etched by the redox reaction. After washing, metallic K and K compounds are removed and pores are created.

The pore size distribution of the APEs measured by the H-K model (supplied by the Beishide 3H-2000PS2 specific surface and pore size analysis instrument) is shown in Figure 5(b). The pore size of the APEs is mainly at a range of 0.5–1.0 nm, implying that massive micropores are present in the APEs. In the aqueous solution of KOH, the micropores

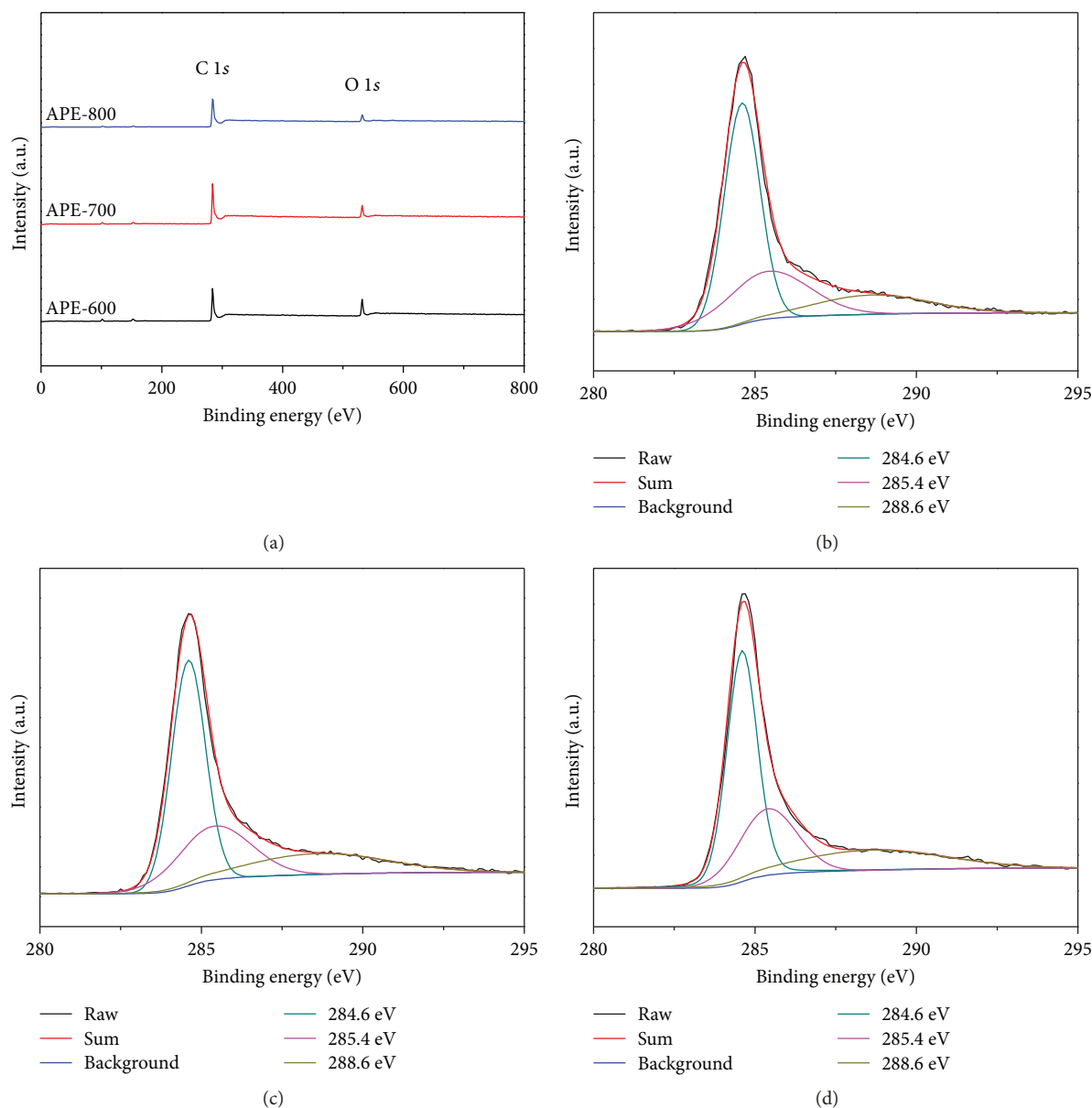


FIGURE 4: (a) XPS spectra of APEs activated at different temperatures. High-resolution C 1s spectra of APE activated at 600°C (b), 700°C (c), and 800°C (d).

TABLE 1: Chemical compositions of as-prepared APEs by XPS analysis.

Element	APE-600	APE-700	APE-800
C (atom%)	82.67	88.96	91.09
O (atom%)	17.33	11.04	8.91

with pore sizes larger than 2 nm are commonly considered too wide to form the double layer while pore sizes less than 0.5 nm are too small for the process [20]. Therefore, it is expected that the pore size of the APEs activated at different temperatures is suitable for the transport of electrolyte ions.

Typical CV curves of the samples with different activation temperatures at the scan rate of $50 \text{ mV}\cdot\text{s}^{-1}$ are shown

in Figure 6(a). It is clear that all CV curves display rectangular-like shapes with a characteristic feature of a good capacitor behavior, promising to be used as the electrode material of supercapacitors. Figure 6(b) presents the GCD curves of APEs measured at a current density of $2 \text{ A}\cdot\text{g}^{-1}$. It is found that the APE-700 has the largest integrated area in the CV curves and the longest charge-discharge time, suggesting the highest specific capacitance for APE-700. Its specific capacitance is calculated as $236 \text{ F}\cdot\text{g}^{-1}$. The Nyquist plots of APEs measured from 10 mHz to 100 kHz are shown in Figure 6(c). APEs display good capacitive behavior with a nearly vertical line at low frequencies, among which the slopes are much larger when the activation temperature decreases. At high frequencies, the intercept of plots with the real axis presents a low equivalent serial

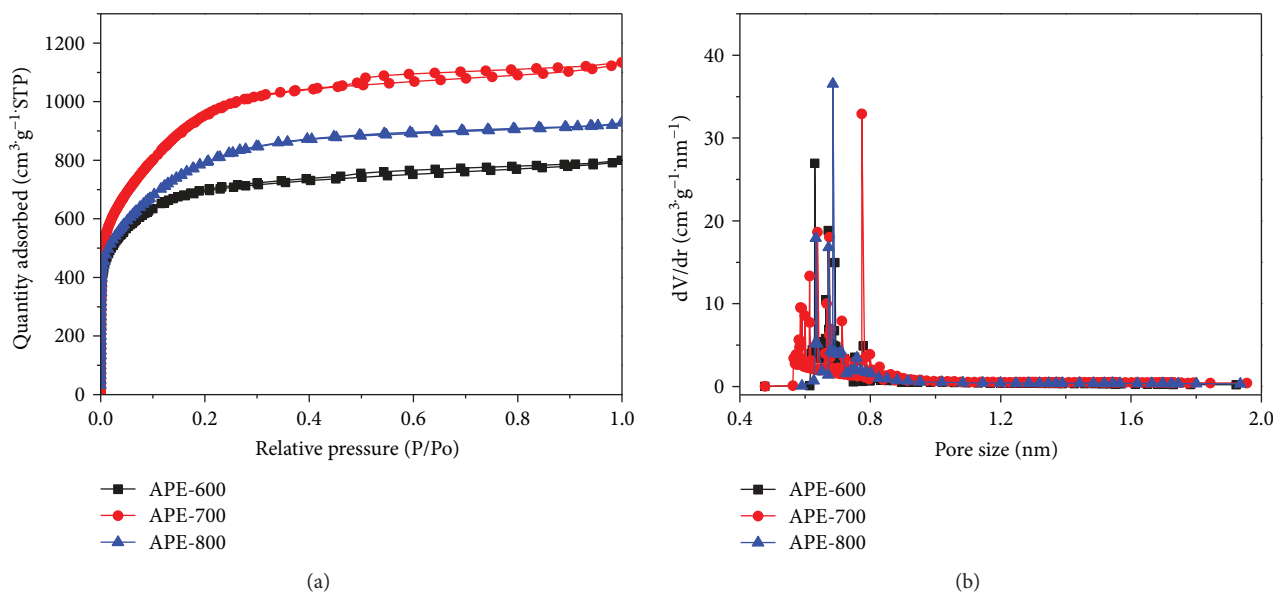


FIGURE 5: (a) Nitrogen adsorption-desorption isotherms of APEs activated at 600°C, 700°C, and 800°C, respectively. (b) Pore size distribution curves of the APEs.

internal resistance of $\sim 0.3 \Omega$, including the intrinsic resistance of activated materials, electrolyte and the contact resistance. The bode phase diagrams of all samples are shown in Figure 6(d). Compared with APE-800, the phase angles of APE-600 and APE-700 are $\sim 85^\circ$ and $\sim 81^\circ$, respectively, which are closed to that of an ideal capacity (90°), indicating a good capacitive property.

The electrochemistry properties of APE-700 have been investigated further in more detail. The CV curves of APE-700 are presented in Figure 6(e) at scan rates from 5 to $100 \text{ mV}\cdot\text{s}^{-1}$. The rectangular-like shape is maintained even at a high scan rate of $100 \text{ mV}\cdot\text{s}^{-1}$, revealing low equivalent series resistance and fast charge transport capability [34]. The GCD curves of APE-700 (Figure 6(f)) show almost symmetrical and linear relationship at a series of current densities ranging from 2 to $20 \text{ A}\cdot\text{g}^{-1}$, which agreed well to a typical property of electrical double-layer capacitors. However, the rate capability of APE-700 is not high, due to abundant micropores and a small amount of mesopores generated by KOH activation. In general, at low current density, the ions of electrolyte are able to penetrate into the micropores. When the current density increases, the narrow micropores may hinder or restrict the ion diffusion due to the space limitations, leading to a moderate rate capability [1, 35].

Table 2 summarizes a comparison of our result with other biomass-derived carbon materials reported previously. It seems that the APE-700 presents a moderate specific capacitance due to its highest surface area. The main reasons are probably as follows: firstly, the specific capacitance is related not only to the surface area but also to the pore structure, interfacial wettability, and electrical conductivity. Secondly, the measurement and electrolyte of the materials listed in Table 2 are not exactly the same. In particular, the specific capacitance would decay when the current density increases.

In order to investigate the practical electrochemical performance of APE-700, the symmetric supercapacitor was assembled and measured in 6M KOH electrolyte. The CV and GCD curves are shown in Figures 7(a) and 7(b). Good capacitive behaviors at different scan rates and current densities are seen. According to (1), the specific capacitance of APE-700 is calculated as $195 \text{ F}\cdot\text{g}^{-1}$ at a current density of $0.2 \text{ A}\cdot\text{g}^{-1}$. Furthermore, the cycling stability of APE-700 was performed by the GCD test at a constant density of $2 \text{ A}\cdot\text{g}^{-1}$. As shown in Figure 7(c), the specific capacitance retention is about 93% with a slight fluctuation after 15000 cycles, exhibiting excellent long-term cycle stability and great potential for energy storage devices.

Figure 7(d) shows the electrochemical impedance spectra of APE-700. It is noted that the equivalent serial internal resistance increases after 15000 cycles, which may be attributed to the abscission of the activated material or the variation of oxygen-containing functional groups. The semicircle loop (nearly 1Ω), an indicator of the charge-transfer resistance between electrolytes and electrode, represents good and stable ionic conductivity of the two samples. The SEM images of APE-700 before and after the cyclic stability test are shown in Figures 8(a) and 8(b). No obvious difference is observed between the two samples.

In summary, *Pleurotus eryngii* activated at 700°C presents a high electrochemistry performance, which may be attributed to the following properties: (a) high specific surface area, which is much more favored to form considerable electrochemical double layers; (b) suitable pore size, which could facilitate ion transport resulting in an effective improvement in the charge-discharge process; (c) high graphitization degree, leading to a good electrical conductivity; and (d) the existence of oxygen-containing functional groups, which not only provides extra pseudo-capacitance but also improves the hydrophilicity and wettability of the porous carbon materials.

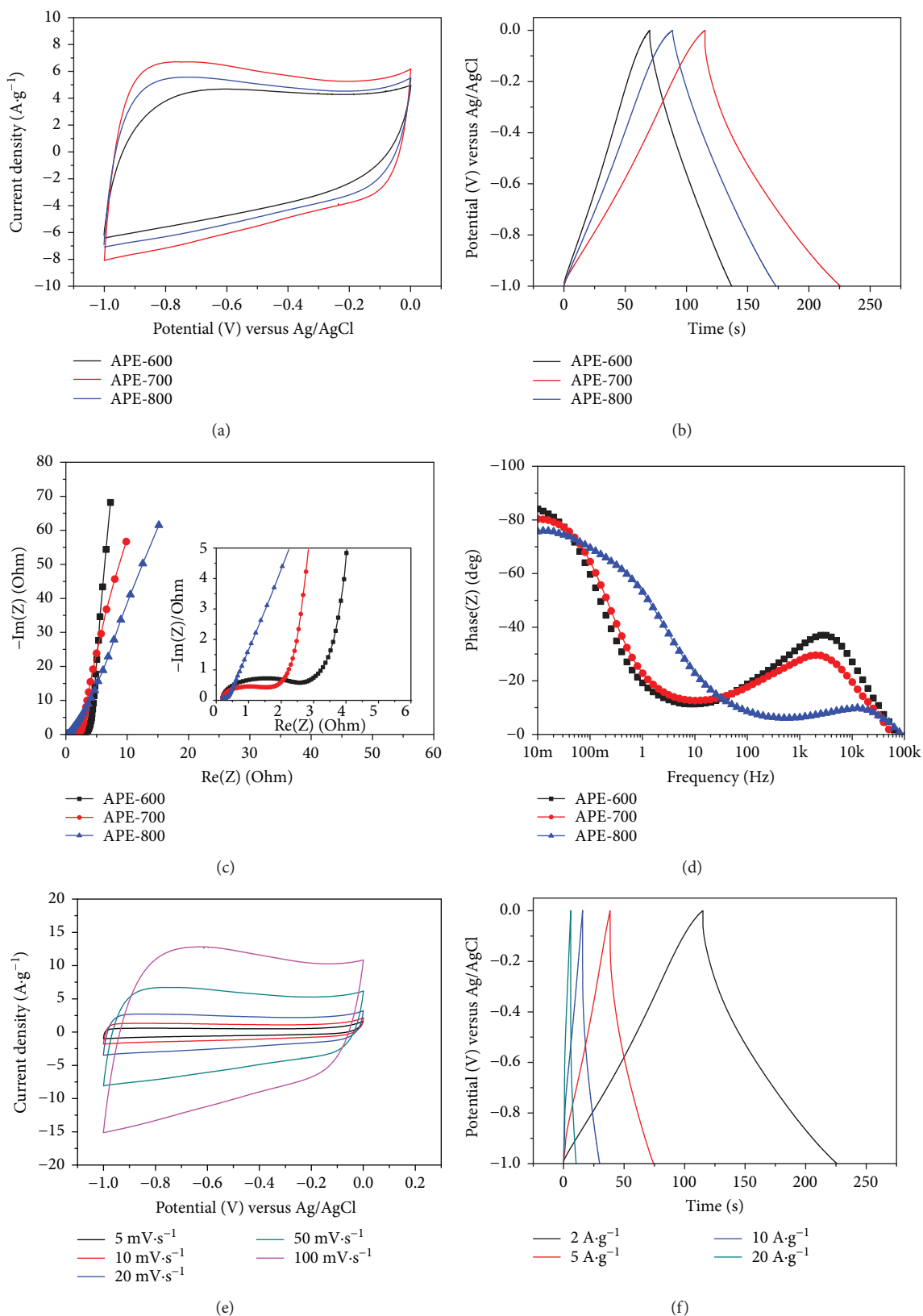


FIGURE 6: Electrochemical performance measured in a three-electrode system: (a) CV curves of APEs activated at 600°C, 700°C, and 800°C, respectively, at $50 \text{ mV}\cdot\text{s}^{-1}$; (b) GCD curves of the APEs at $2 \text{ A}\cdot\text{g}^{-1}$; (c) Nyquist plots of the APEs, an enlarged view in the high-frequency region is shown in the inset; (d) bode phase diagrams of the APEs; (e) CV curves of APE-700 at different scan rates from 5 to $100 \text{ mV}\cdot\text{s}^{-1}$; (f) GCD curves of APE-700 at different current densities from 2 to $20 \text{ A}\cdot\text{g}^{-1}$.

TABLE 2: Comparison of the properties of biomass-derived carbon materials.

Biomass	S_{BET} ($\text{m}^2 \cdot \text{g}^{-1}$)	C_m ($\text{F} \cdot \text{g}^{-1}$)	Measurement	Electrolyte	Ref.
Willow catkins	1533	298	$0.5 \text{ A} \cdot \text{g}^{-1}$	6 M KOH	[16]
Tea leave	2841	330	$1 \text{ A} \cdot \text{g}^{-1}$	2 M KOH	[21]
Glucose	757	260	$0.5 \text{ A} \cdot \text{g}^{-1}$	6 M KOH	[17]
Coconut shell	1532	228	$5 \text{ mV} \cdot \text{s}^{-1}$	6 M KOH	[19]
Corn starch	1167	162	$0.625 \text{ A} \cdot \text{g}^{-1}$	6 M KOH	[18]
Cotton	1085	207	$1 \text{ A} \cdot \text{g}^{-1}$	1 M H_2SO_4	[28]
Paulownia sawdust	1900	227	$2 \text{ mV} \cdot \text{s}^{-1}$	6 M KOH	[36]
APE-700	3255	236	$2 \text{ A} \cdot \text{g}^{-1}$	6 M KOH	This work

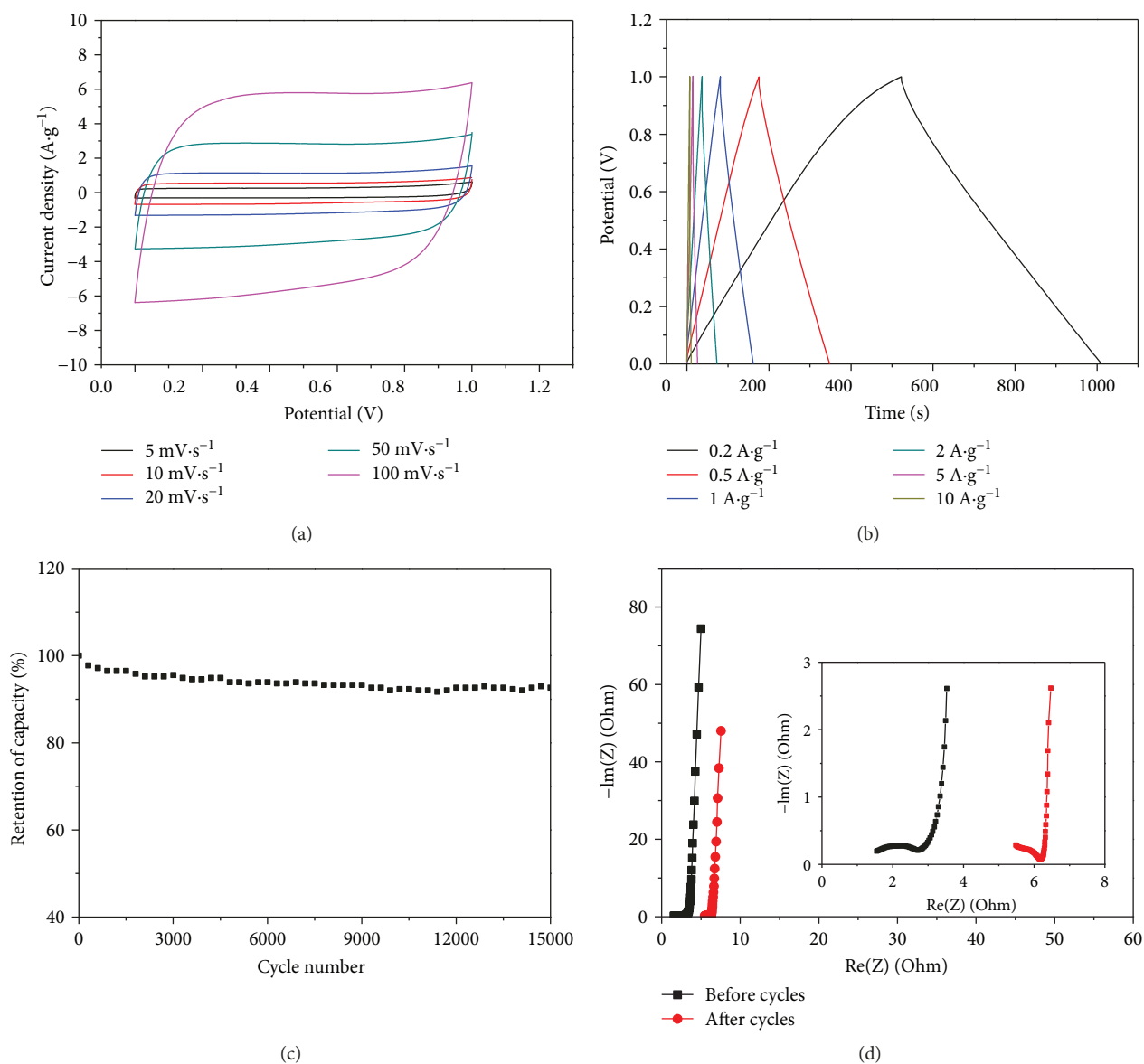


FIGURE 7: Electrochemical performance of APE-700 measured in a two-electrode system: (a) CV curves at different scan rates from 5 to 100 $\text{mV} \cdot \text{s}^{-1}$; (b) GCD curves at different current densities from 0.2 to 10 $\text{A} \cdot \text{g}^{-1}$; (c) cycle stability at a current density of 2 $\text{A} \cdot \text{g}^{-1}$ in 6 M KOH solution; (d) EIS before and after the cyclic stability test, an enlarged view in the high-frequency region is shown in the inset.

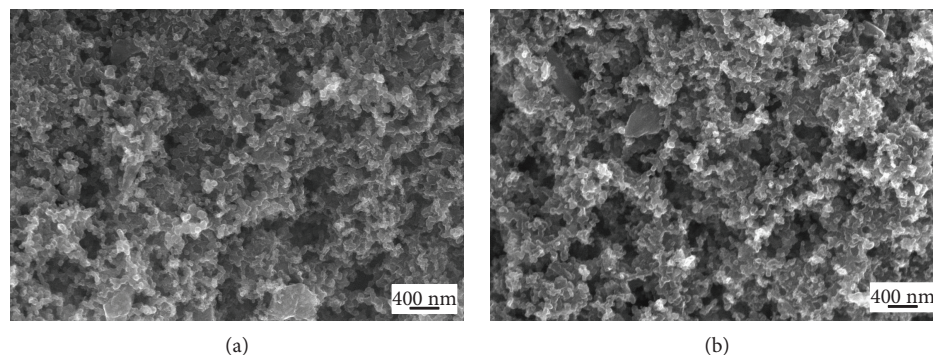


FIGURE 8: SEM images of APE-700 (a) before the cyclic stability test and (b) after the cyclic stability test.

4. Conclusion

Porous activated carbons derived from *Pleurotus eryngii* were synthesized by carbonization firstly and then KOH activation. The porous carbons activated at 700°C, among other activation temperatures, exhibit the highest specific surface area of 3255 m²·g⁻¹, and the prepared electrode offers a maximal specific capacitance of 236 F·g⁻¹ measured in a three-electrode cell system. Furthermore, the assembled symmetric supercapacitor shows a specific capacitance of 195 F·g⁻¹ at 0.2 A·g⁻¹ and excellent long-term cycle stability with a capacitance retention of 93% after 15000 charge/discharge cycles at a current density of 2 A·g⁻¹. This work highlights the attractive capacitive features of the *Pleurotus eryngii* as a readily available biomass source, which might inspire their future development as a new resource of porous activated carbons for supercapacitors and other energy storage devices.

Conflicts of Interest

The authors declare that they have no conflicts of interest.

Acknowledgments

This work was supported by the National Natural Science Foundation of China (NSFC Grant 21750110441), Jiangsu Human Resource and Social Security Grant (2014-XCL-038), Suzhou Science and Technology Programme (SYG 201623), Suzhou Industrial Park Initiative Platform Development for Suzhou Municipal Key Lab for New Energy Technology (RR0140), Guangdong Research Center for Interfacial Engineering of Functional Materials (201701), Key Program Special Fund in XJTU (KSF-P-02, KSF-A-04, KSF-A-05 and KSF-A-07), and the XJTU Research Development Fund (RDF-14-02-42 and RDF-17-01-13).

References

- [1] A. G. Pandolfo and A. F. Hollenkamp, "Carbon properties and their role in supercapacitors," *Journal of Power Sources*, vol. 157, no. 1, pp. 11–27, 2006.
- [2] D. Pech, M. Brunet, H. Durou et al., "Ultrahigh-power micrometre-sized supercapacitors based on onion-like carbon," *Nature Nanotechnology*, vol. 5, no. 9, pp. 651–654, 2010.
- [3] A. Nishino, "Capacitors: operating principles, current market and technical trends," *Journal of Power Sources*, vol. 60, no. 2, pp. 137–147, 1996.
- [4] C.-M. Chen, Q. Zhang, C. H. Huang et al., "Macroporous 'bubble' graphene film via template-directed ordered-assembly for high rate supercapacitors," *Chemical Communications*, vol. 48, no. 57, pp. 7149–7151, 2012.
- [5] Y. S. Yun, G. Yoon, K. Kang, and H.-J. Jin, "High-performance supercapacitors based on defect-engineered carbon nanotubes," *Carbon*, vol. 80, pp. 246–254, 2014.
- [6] D. T. Pham, T. H. Lee, D. H. Luong et al., "Carbon nanotube-bridged graphene 3D building blocks for ultrafast compact supercapacitors," *ACS Nano*, vol. 9, no. 2, pp. 2018–2027, 2015.
- [7] Q. Liao, N. Li, S. Jin, G. Yang, and C. Wang, "All-solid-state symmetric supercapacitor based on Co₃O₄ nanoparticles on vertically aligned graphene," *ACS Nano*, vol. 9, no. 5, pp. 5310–5317, 2015.
- [8] L. Liu, J. Lang, P. Zhang, B. Hu, and X. Yan, "Facile synthesis of Fe₂O₃ nano-dots @ nitrogen-doped graphene for supercapacitor electrode with ultralong cycle life in KOH electrolyte," *ACS Applied Materials & Interfaces*, vol. 8, no. 14, pp. 9335–9344, 2016.
- [9] S. A. Ansari, H. Fouad, S. G. Ansari, M. P. Sk, and M. H. Cho, "Mechanically exfoliated MoS₂ sheet coupled with conductive polyaniline as a superior supercapacitor electrode material," *Journal of Colloid and Interface Science*, vol. 504, pp. 276–282, 2017.
- [10] L. Ma, R. Liu, H. Niu, M. Zhao, and Y. Huang, "Flexible and freestanding electrode based on polypyrrole/graphene/bacterial cellulose paper for supercapacitor," *Composites Science and Technology*, vol. 137, pp. 87–93, 2016.
- [11] Y. Han, Y. Ge, Y. Chao, C. Wang, and G. G. Wallace, "Recent progress in 2D materials for flexible supercapacitors," *Journal of Energy Chemistry*, vol. 27, no. 1, pp. 57–72, 2018.
- [12] L.-F. Chen, Z.-H. Huang, H.-W. Liang, Q.-F. Guan, and S.-H. Yu, "Bacterial-cellulose-derived carbon nanofiber@MnO₂ and nitrogen-doped carbon nanofiber electrode materials: an asymmetric supercapacitor with high energy and power density," *Advanced Materials*, vol. 25, no. 34, pp. 4746–4752, 2013.
- [13] K. Krishnamoorthy and S. J. Kim, "Mechanochemical preparation of graphene nanosheets and their supercapacitor applications," *Journal of Industrial and Engineering Chemistry*, vol. 32, pp. 39–43, 2015.

- [14] L.-F. Chen, Y. Feng, H.-W. Liang, Z.-Y. Wu, and S.-H. Yu, "Macroscopic-scale three-dimensional carbon nanofiber architectures for electrochemical energy storage devices," *Advanced Energy Materials*, vol. 7, no. 23, article 1700826, 2017.
- [15] J. Deng, M. Li, and Y. Wang, "Biomass-derived carbon: synthesis and applications in energy storage and conversion," *Green Chemistry*, vol. 18, no. 18, pp. 4824–4854, 2016.
- [16] Y. Li, G. Wang, T. Wei, Z. Fan, and P. Yan, "Nitrogen and sulfur co-doped porous carbon nanosheets derived from willow catkin for supercapacitors," *Nano Energy*, vol. 19, pp. 165–175, 2016.
- [17] J. Wang, L. Shen, B. Ding et al., "Fabrication of porous carbon spheres for high-performance electrochemical capacitors," *RSC Advances*, vol. 4, no. 15, pp. 7538–7544, 2014.
- [18] L. Pang, B. Zou, X. Han, L. Cao, W. Wang, and Y. Guo, "One-step synthesis of high-performance porous carbon from corn starch for supercapacitor," *Materials Letters*, vol. 184, pp. 88–91, 2016.
- [19] J. Mi, X. R. Wang, R. J. Fan, W. H. Qu, and W. C. Li, "Coconut-shell-based porous carbons with a tunable micro/mesopore ratio for high-performance supercapacitors," *Energy & Fuels*, vol. 26, no. 8, pp. 5321–5329, 2012.
- [20] K. Wang, N. Zhao, S. Lei et al., "Promising biomass-based activated carbons derived from willow catkins for high performance supercapacitors," *Electrochimica Acta*, vol. 166, pp. 1–11, 2015.
- [21] C. Peng, X. B. Yan, R. T. Wang, J. W. Lang, Y. J. Ou, and Q. J. Xue, "Promising activated carbons derived from waste tea-leaves and their application in high performance supercapacitors electrodes," *Electrochimica Acta*, vol. 87, pp. 401–408, 2013.
- [22] S. Gao, Y. Chen, H. Fan et al., "Large scale production of biomass-derived N-doped porous carbon spheres for oxygen reduction and supercapacitors," *Journal of Materials Chemistry A*, vol. 2, no. 10, pp. 3317–3324, 2014.
- [23] P. Cheng, S. Gao, P. Zang et al., "Hierarchically porous carbon by activation of shiitake mushroom for capacitive energy storage," *Carbon*, vol. 93, pp. 315–324, 2015.
- [24] P. Yadav, A. Basu, A. Suryawanshi, O. Game, and S. Ogale, "Highly stable laser-scribed flexible planar microsupercapacitor using mushroom derived carbon electrodes," *Advanced Materials Interfaces*, vol. 3, no. 11, article 1600057, 2016.
- [25] L. Yao, G. Yang, P. Han, Z. Tang, and J. Yang, "Three-dimensional beehive-like hierarchical porous polyacrylonitrile-based carbons as a high performance supercapacitor electrodes," *Journal of Power Sources*, vol. 315, pp. 209–217, 2016.
- [26] W. K. Chee, H. N. Lim, Z. Zainal, N. M. Huang, I. Harrison, and Y. Andou, "Flexible graphene-based supercapacitors: a review," *Journal of Physical Chemistry C*, vol. 120, no. 8, pp. 4153–4172, 2016.
- [27] C.-S. Yang, Y. S. Jang, and H. K. Jeong, "Bamboo-based activated carbon for supercapacitor applications," *Current Applied Physics*, vol. 14, no. 12, pp. 1616–1620, 2014.
- [28] L. Li, Q. Zhong, N. D. Kim et al., "Nitrogen-doped carbonized cotton for highly flexible supercapacitors," *Carbon*, vol. 105, pp. 260–267, 2016.
- [29] T. I. T. Okpalugo, P. Papakonstantinou, H. Murphy, J. McLaughlin, and N. M. D. Brown, "High resolution XPS characterization of chemical functionalised MWCNTs and SWCNTs," *Carbon*, vol. 43, no. 1, pp. 153–161, 2005.
- [30] Q. Wang, Q. Cao, X. Wang, B. Jing, H. Kuang, and L. Zhou, "A high-capacity carbon prepared from renewable chicken feather biopolymer for supercapacitors," *Journal of Power Sources*, vol. 225, pp. 101–107, 2013.
- [31] J. Yin, D. Zhang, J. Zhao, X. Wang, H. Zhu, and C. Wang, "Meso- and micro-porous composite carbons derived from humic acid for supercapacitors," *Electrochimica Acta*, vol. 136, pp. 504–512, 2014.
- [32] Z. Hu, M. P. Srinivasan, and Y. Ni, "Preparation of mesoporous high-surface-area activated carbon," *Advanced Materials*, vol. 12, no. 1, pp. 62–65, 2000.
- [33] J. Wang and S. Kaskel, "KOH activation of carbon-based materials for energy storage," *Journal of Materials Chemistry*, vol. 22, no. 45, pp. 23710–23725, 2012.
- [34] J. Zhi, W. Zhao, X. Liu, A. Chen, Z. Liu, and F. Huang, "Highly conductive ordered mesoporous carbon based electrodes decorated by 3D graphene and 1D silver nanowire for flexible supercapacitor," *Advanced Functional Materials*, vol. 24, no. 14, pp. 2013–2019, 2014.
- [35] W. Xing, C. C. Huang, S. P. Zhuo et al., "Hierarchical porous carbons with high performance for supercapacitor electrodes," *Carbon*, vol. 47, no. 7, pp. 1715–1722, 2009.
- [36] X. Liu, M. Zheng, Y. Xiao et al., "Microtube bundle carbon derived from paulownia sawdust for hybrid supercapacitor electrodes," *ACS Applied Materials & Interfaces*, vol. 5, no. 11, pp. 4667–4677, 2013.



Hindawi
Submit your manuscripts at
www.hindawi.com

